

Supplemental data

Construction of a self-supporting bifunctional Sn-SnS_x electrocatalyst via one-step electrodeposition for formate production from coupled CO₂ reduction and glucose oxidation

Chongyan Chen^{1,a}, Shuguang Shen^{1,a,*}, Jie Wang^a, Yongmei Liu^a, Xingting Guo^a, Lili
Zhang^a, Jing Li^a

¹The two authors contributed equally to this work and should be considered co-first
authors.

^aCollege of Chemical Engineering and Technology, Taiyuan University of
Technology, Taiyuan, 030024, China

***Corresponding Author:** Mr. Shuguang Shen

Corresponding author Address: College of Chemical Engineering and Technology,
Taiyuan University of Technology, Taiyuan 030024, China, Tel. (+86)13303511628.

E-mail Address: sgshen@sina.com

Characterizations

The morphologies of the catalyst were analyzed by the scanning electron microscopy (SEM, ZEISS Gemini 300). The X-ray diffraction (XRD) patterns were recorded on a Smartlab SE X-ray diffractometer using Cu -K α radiation ($\lambda = 0.15405$ nm). The X-ray photoelectron spectroscopy (XPS) was carried out on a Thermo Scientific K-Alpha. An Al-K α X-ray source was used with power of 72 W (6 mA and 12 kV), and the 400 μ m X-ray spot was used to acquire XPS spectra. The C1s peak (284.8 eV) was used as the standard for charge calibration. The peak resolution and fitting were processed by Avantage software. The Schofield coefficient is 37.257 for the Sn element, 1.881 for the S element, and 26.513 for the Cu element. The ^1H and ^{13}C NMR spectra were collected on a Bruker 400 MHz spectrometer. The NMR samples were prepared by mixing the electrolyte with D $_2$ O. The presaturation method was used to suppress the water peak. Inductively coupled plasma optical emission spectrometry (ICP-OES) measurements were conducted on an Agilent 5110 spectrometer. Transmission electron microscopy (TEM, FEI Talos F200S) was applied to study the microstructure of the sample. Electrochemical measurements were performed on a CHI660E electrochemical workstation (Shanghai, China).

Electrochemical Measurements

The CO $_2$ RR and GOR performance of Sn-SnS $_x$ electrode were performed in a commercial H-type electrolyzer separating by a cation exchange membrane (Nafion 117). The Ag/AgCl electrode, platinum plate (1 \times 1 cm 2) and Sn-SnS $_x$ (1 \times 1 cm 2) act as the reference electrode, counter electrode, and work electrode, respectively. For CO $_2$ RR, 50 mL 0.1 M KHCO $_3$ aqueous solution was used as catholyte. For GOR, 50 mL 0.1 M KOH and 0.1 M glucose aqueous solution were used as anolyte. Before electrolysis, the cathode electrolyte was bubbled with CO $_2$ at least 30 min with a flow rate of 30 mL min $^{-1}$.

All potentials were measured with the Ag/AgCl reference electrode and converted to the reversible hydrogen electrode (RHE) according to the Eq. (1):

$$E(\text{vs. RHE}) = E(\text{vs. Ag/AgCl}) + 0.197 \text{ V} + 0.059 \text{ V} \times \text{pH} \dots \dots \dots (1)$$

LSV: Cyclic voltammetry (CV) was repeatedly carried out before other tests until stable CV curves were observed. The linear sweep voltammetry (LSV) test at cathode was performed in the CO₂ or N₂ saturated 0.1 M KHCO₃ aqueous solution at a scan rate of 5 mV s⁻¹. The LSV test at anode was performed in the aqueous solution with and without 0.1 M glucose at a scan rate of 5 mV s⁻¹.

Tafel plot: The current-potential data were obtained by LSV at a scan rate of 0.1 mV/s. The Tafel slope was obtained from the LSV curve using a linear fit applied to points in the Tafel region.

EIS: The electrochemical impedance spectroscopy (EIS) was measured over a frequency range of 0.01 Hz to 100 kHz, applying a sinusoidal voltage with an amplitude of 5 mV at open-circuit potential (OCP).

C_{dl}: A series of CV experiments were conducted on the voltage range of 0 - -0.1 V vs. RHE at different scan rates of 20, 40, 60, 80, 100, and 120 mV/s. Linear fitting was performed with scanning speed (mV/s) as the x-axis and Δ*j* (mA/cm²) as the y-axis, and the slope of the curve was the double-layer capacitance C_{dl} (mF/cm²).

Product Quantification

The HPLC was also conducted on EasySep-3030 with a UV-Vis detector to determine and analyze the **formate** in the solutions. 5 mM H₃PO₄ solution was used as the mobile phase with a constant flow rate of 1 mL/min.

The Faradaic efficiencies (FEs) for the liquid product in GOR and CO₂RR were calculated using Eq. (2):

$$\text{FE} (\%) = n m F/Q \times 100\% \dots \dots \dots (2)$$

n is the number of exchanged electrons to form 1 mol formate, 2 for CO₂RR and 2 for GOR. *m* is the amount of formate calculated from high performance liquid chromatography (HPLC) (mol). *F* is the Faradaic constant (96485 C/mol); *Q* is the total charge flowing through the electrode surface (C).

Analysis of **CO** and **H₂** was conducted on gas chromatograph HXSP GC-950 equipped with Flame Ionization Detector (FID) and thermal conductivity detector (TCD) using Ar as carrier gas. FE for the gas product in CO₂RR was calculated according to Eq. (3):

$$FE (\%) = n P V v_i F / R T Q \times 100\% \dots\dots\dots(3)$$

n is the number of exchanged electrons to CO or H₂; *P* is atmospheric pressure (101325 Pa); *V* is the volume flow rate of the CO₂ supplied to the H-cell throughout electrolysis; *v_i* is the volume fraction of CO or H₂ in the gas sample, which is determined by gas chromatography (GC); *R* is the gas constant (8.314 J·mol⁻¹·K⁻¹); *T* is the temperature (298.15 K).

Glucose quantification

Quantitative analysis of **glucose** was performed using HPLC (Viscotek VE3580) with assembled amino column and RI detector. Xylose served as an internal standard, using a mixture of acetonitrile and water (7:3) as the mobile phase, with a flow rate of 1 ml/min. The glucose conversion was calculated by the following equations:

$$\text{Conversion (\%)} = \text{Moles of carbon in feedstock consumed} / \text{Moles of carbon in feedstock input} \times 100\%$$

Calculation of production rate (PR), energy consumption (W_E) and the energy efficiency of the CO₂RR//GOR cell (EE_{cell}):

PR: The PR (μmol h⁻¹ cm⁻²) of formate produced by CO₂RR or GOR was calculated as follows (4):

$$PR = \frac{c \times V}{t \times S} \times 100\% \quad (4)$$

where *c* is the molar concentration of formate in the electrolyte (μmol L⁻¹); *V* is the volume of the electrolyte (L); *t* is the reaction time (h); *S* is the geometric area of the working electrode (cm²).

W_E: The energy consumption *W_E* (Wh mmol⁻¹_{formate}) of CO₂RR//GOR and

CO₂RR//OER systems can be calculated using formula (5):

$$\text{Energy consumption} = W/m = U \times Q/m \quad (5)$$

where U is the applied cell voltage (1.8 V), Q is the consumed electricity after 1 h of reaction at 1.8 V in the CO₂RR//GOR and CO₂RR//OER system (C), m represents the amount of formate (1461.24 mmol for CO₂RR//GOR and 229.68 mmol for CO₂RR//OER after reaction for 1 h at 1.8 V).

The “**energy savings**” was determined based on the following equation (6):

$$\text{Energy saving} = (WE1 - WE2)/WE1 \times 100\% \quad (6)$$

in which W_{E1} and W_{E2} represent the electric energy consumption in producing per mol of formate in the CO₂RR//OER (0.12Wh mmol⁻¹_{formate}) and CO₂RR//GOR (0.05Wh mmol⁻¹_{formate}) systems, respectively.

The **energy efficiency of the CO₂RR//GOR cell (EE_{cell})** is calculated using the

equation:¹
$$EE_{cell} = \frac{|FE_{\text{formate}}^{\text{cathode}} E_{\text{CO}_2/\text{formate}} - FE_{\text{formate}}^{\text{anode}} E_{\text{glucose/formate}}|}{V_{cell}}$$
 to calculate the energy efficiency (EE_{cell}) of the CO₂RR//GOR cell. Where $E_{\text{CO}_2/\text{formate}}$ and $E_{\text{glucose/formate}}$ represent the reduction potentials for CO₂ and glucose, respectively, under non-standard conditions. The potential value can be calculated using the Nernst equation (Equation 7), and the calculation process is listed in Table S5.

$$E = E^0 - 0.059 \times \text{pH} \quad (7)$$

Among them, E^0 represents the standard potential, $E_{\text{CO}_2/\text{formate}}^0$ can be obtained from literature, and $E_{\text{Cglucose/formate}}^0$ can be calculated based on the standard Gibbs free energy change ΔG_{rxn}^0 (Equation 8):

$$E^0 = -\Delta G_{\text{rxn}}^0/nF \quad (8)$$

where ΔG_{rxn}^0 represents the difference in standard Gibbs free energy, ΔG_f^0 can be obtained from literature. n is the number of transfer electron, and F is the Faraday constant.

Supplementary figures and tables

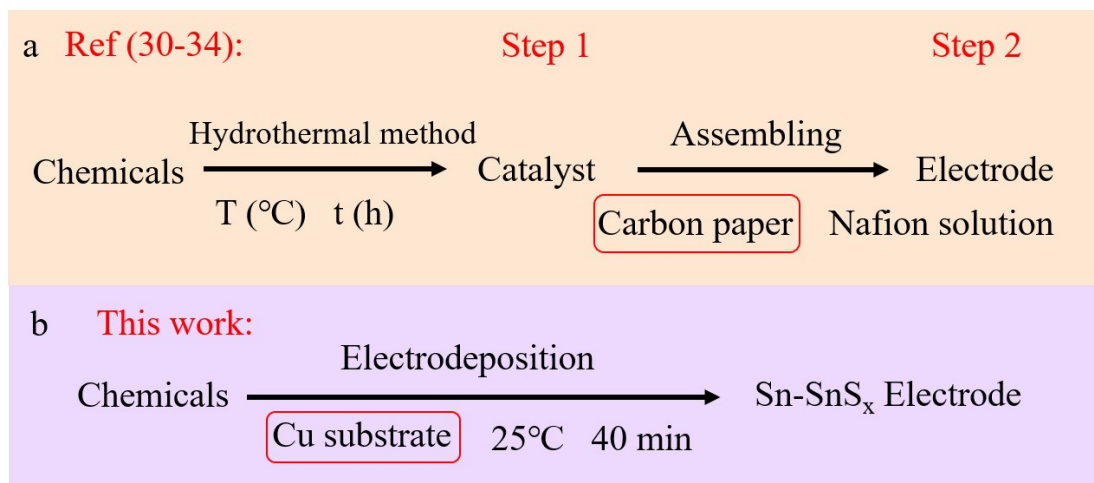


Figure S1. Two step preparation of tin sulfide electrodes (a), Preparation of Sn-SnS_x electrode by one-step in-situ electrodeposition (b).

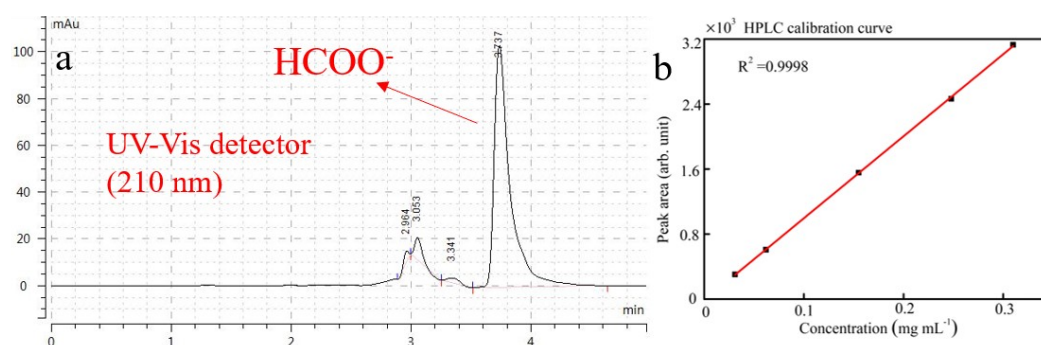


Figure S2. The spectra of HCOO^- product detected by HPLC (a), Calibration curve for HCOO^- (b).

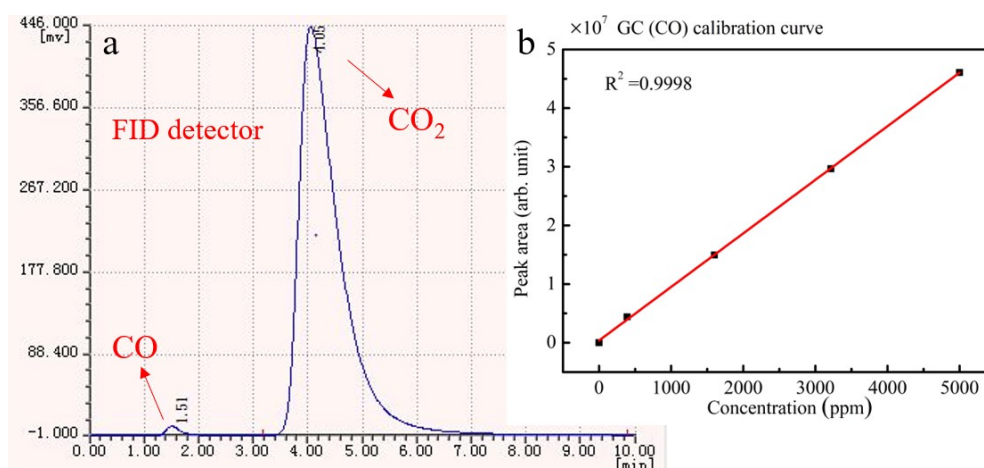


Figure S3. The spectra of CO product detected by GC (a), Calibration curve for CO (b).

(b).

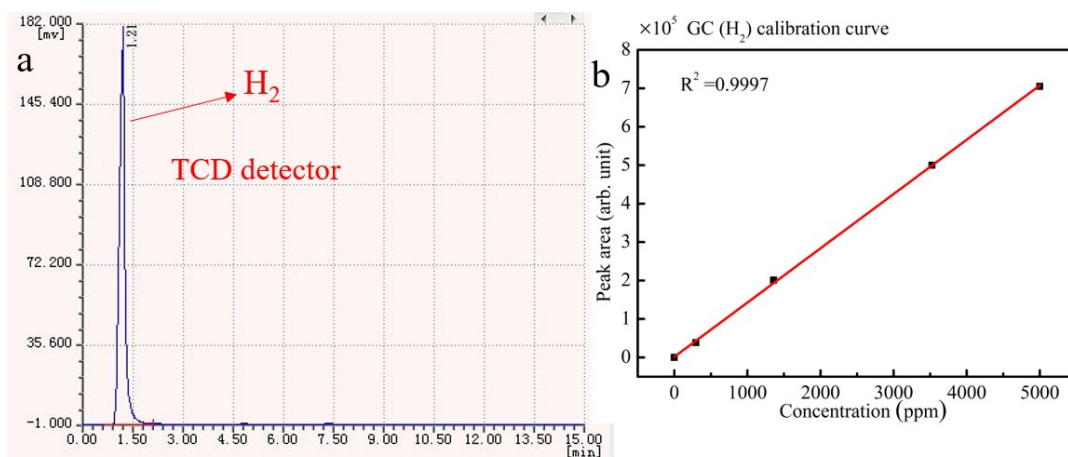


Figure S4. The spectra of H₂ product detected by GC (a), Calibration curve for H₂ (b).

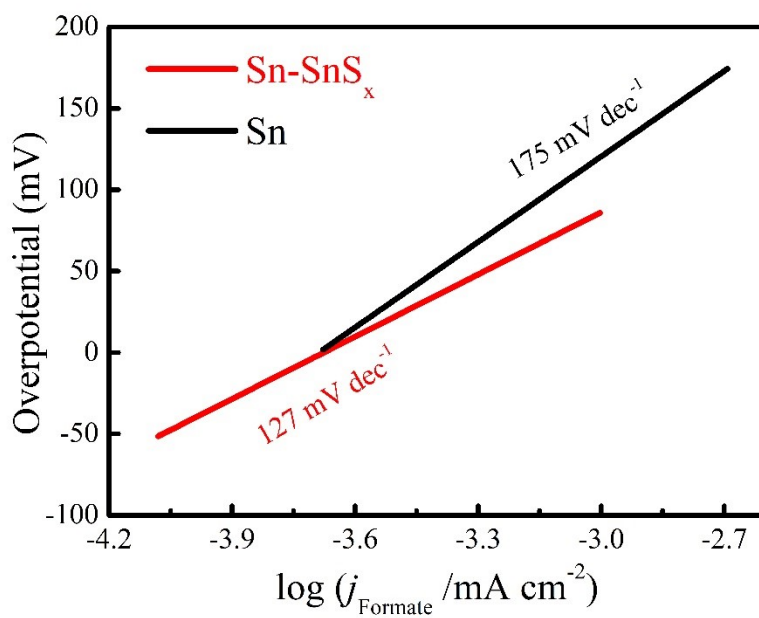


Figure S5. Tafel plots of Sn and Sn-SnS_x electrode.

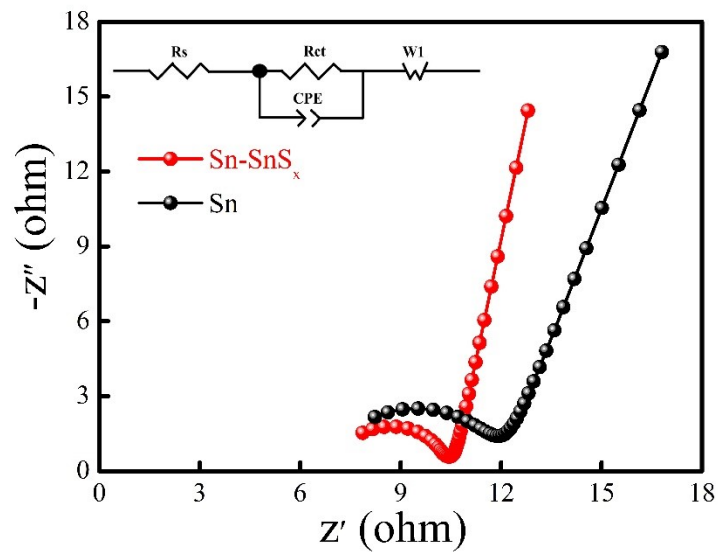


Figure S6. EIS results of Sn (OCP: -225.5 mV) and Sn-SnS_x (OCP: -157.2 mV) electrode.

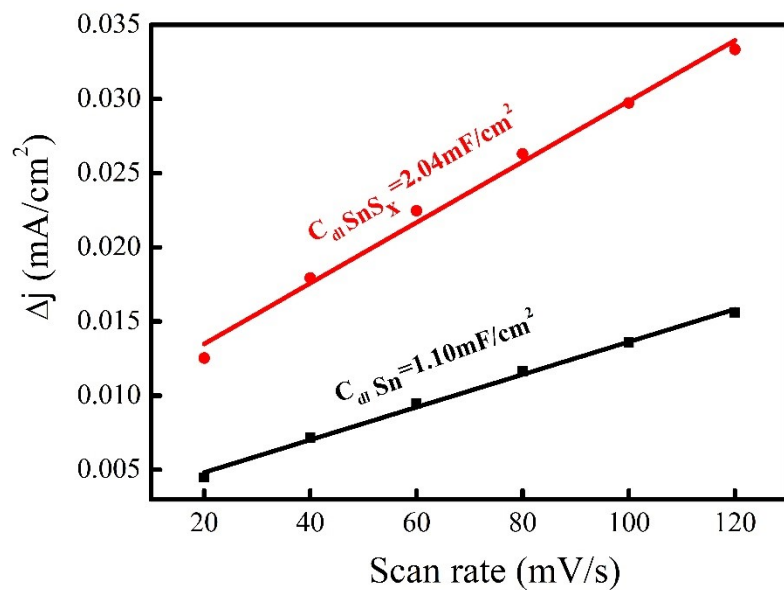


Figure S7. Plots of charging current density difference versus scan rate for Sn and Sn-SnS_x with a fit slope of C_{dl}.

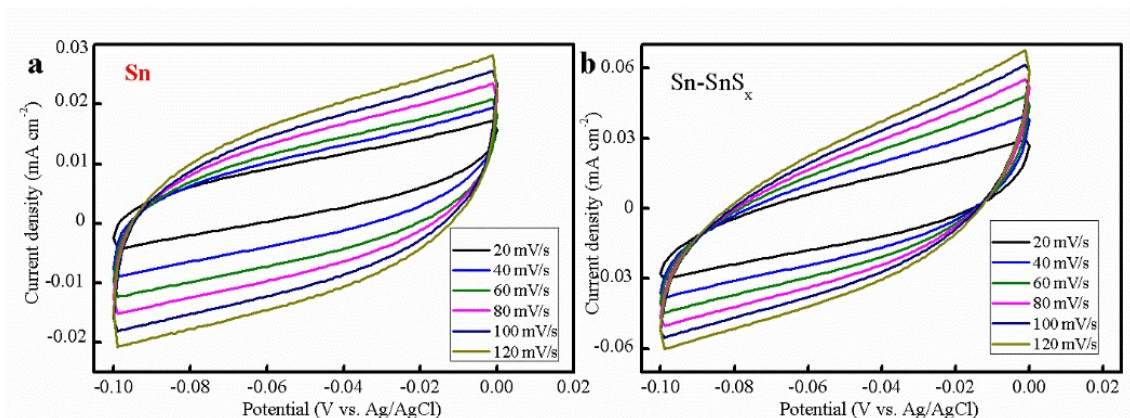


Figure S8. Cyclic voltammetry (CV) curves of Sn (a) and Sn-SnS_x (b) at different scanning speeds.

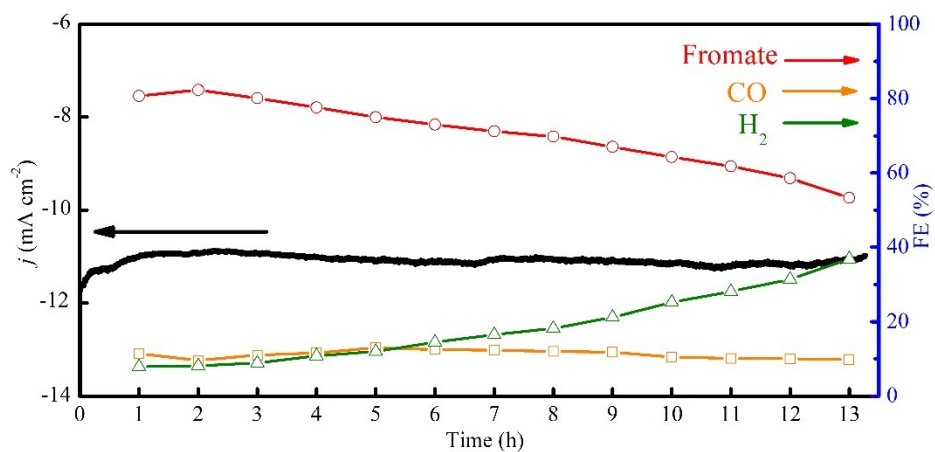


Figure S9. Electrocatalytic durability of Sn during the long-term CO₂ electrolysis at the constant potential of -1.2 V vs. RHE.

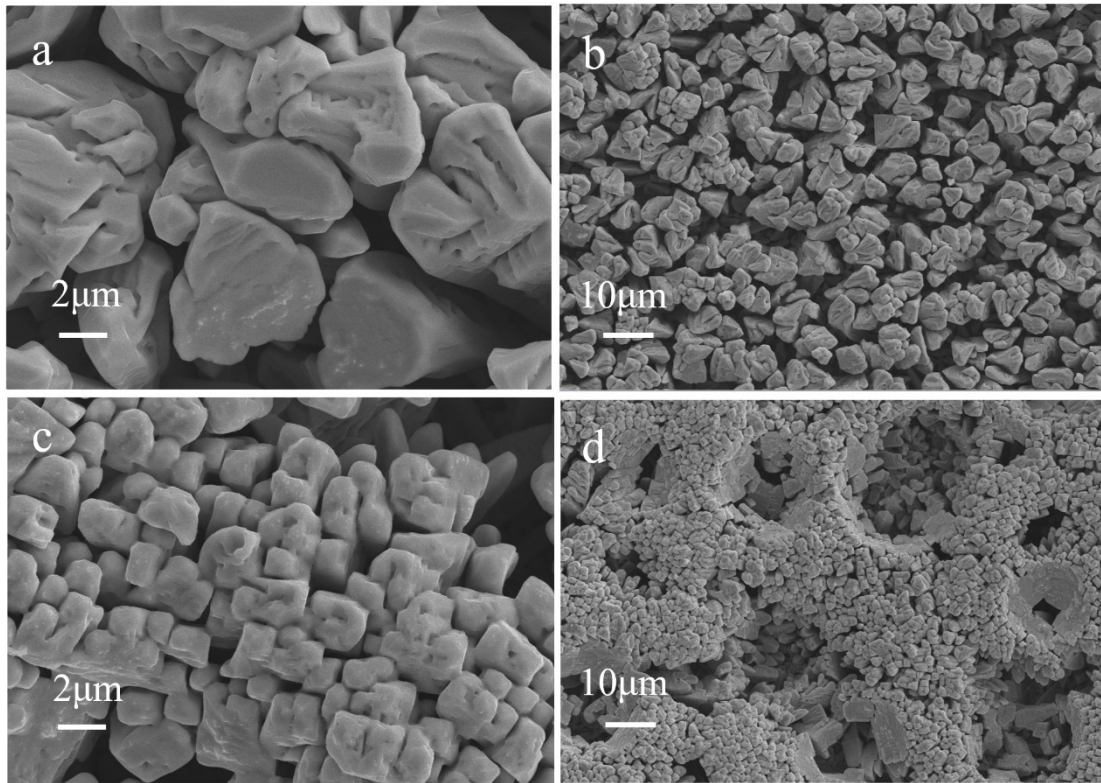


Figure S10. SEM images of Sn electrode before (a,b) and three hours after (c,d) the CO₂RR.

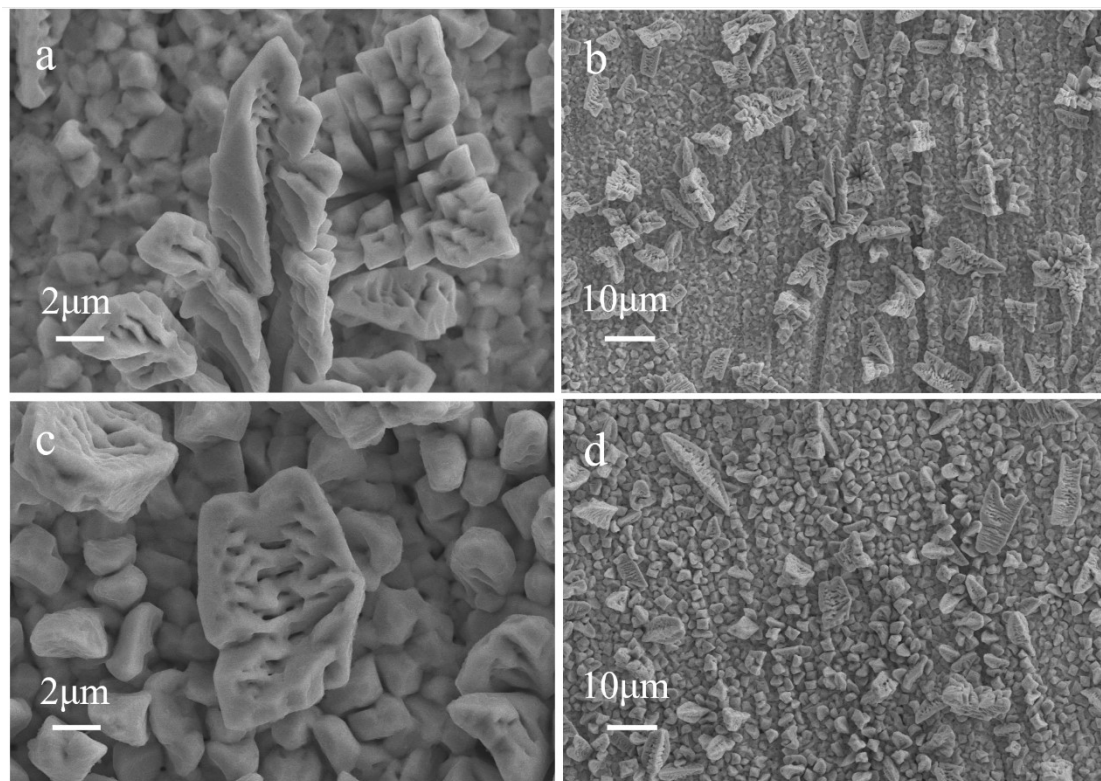


Figure S11. SEM images of Sn-SnS_x electrode before (a, b) and twenty hours after (c, d) the CO₂RR.

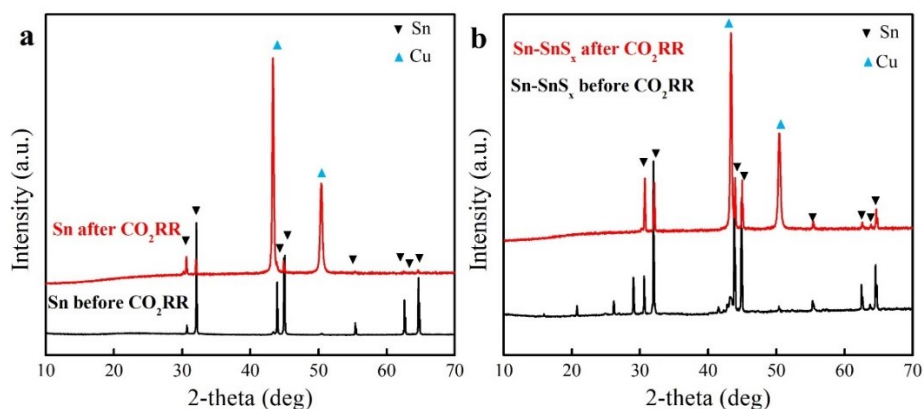


Figure S12. XRD patterns of Sn electrode (a) before and 13 hours after the CO₂RR, Sn-SnS_x (b) electrode before and 36 hours after the CO₂RR.

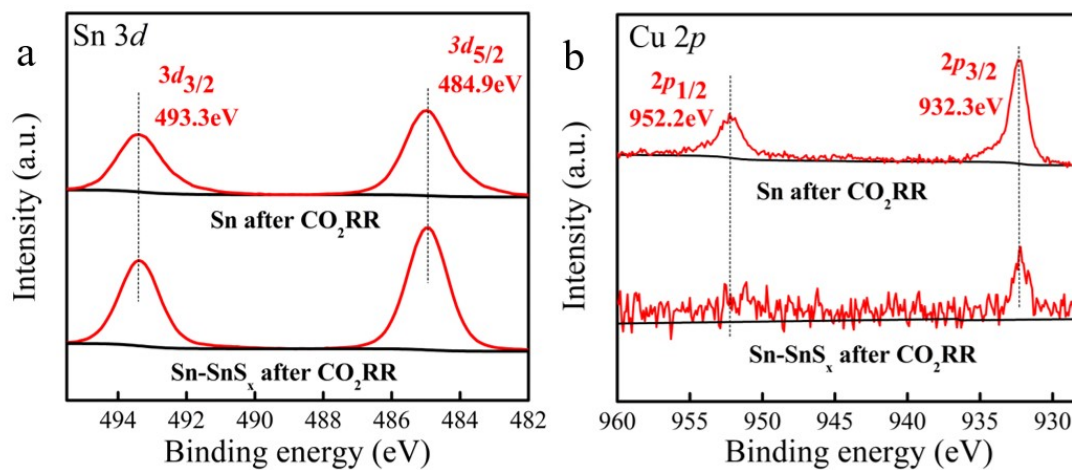


Figure S13. XPS survey spectra of Sn 3d (a), Cu 2p (b) for the Sn and Sn-SnS_x electrodes after the CO₂RR.

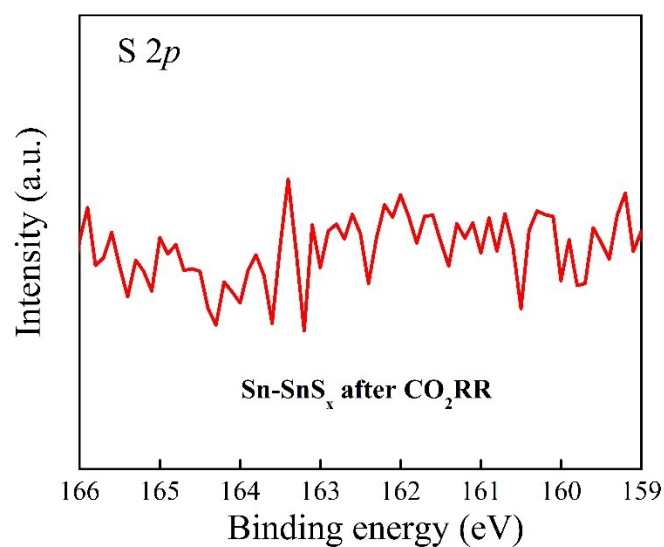


Figure S14. XPS survey spectra of S 2p for the Sn-SnS_x electrode after the CO₂RR.

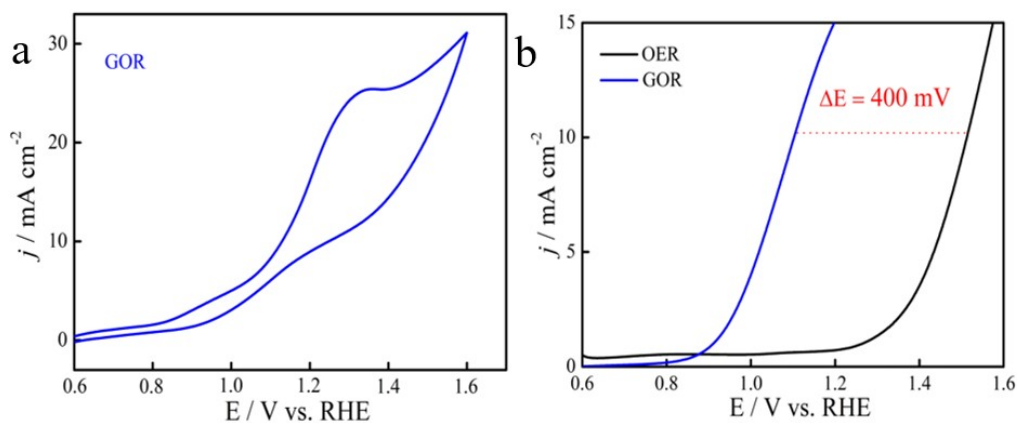


Figure S15. The CV curve (scan rate: 5 mV s^{-1}) of Sn-SnS_x electrode in 0.1 M KOH and 0.1 M glucose aqueous solution (a), LSV curves (scan rate: 5 mV s^{-1}) of Sn-SnS_x electrode with and without the existence of C₆H₁₂O₆ in the anode cell (b).

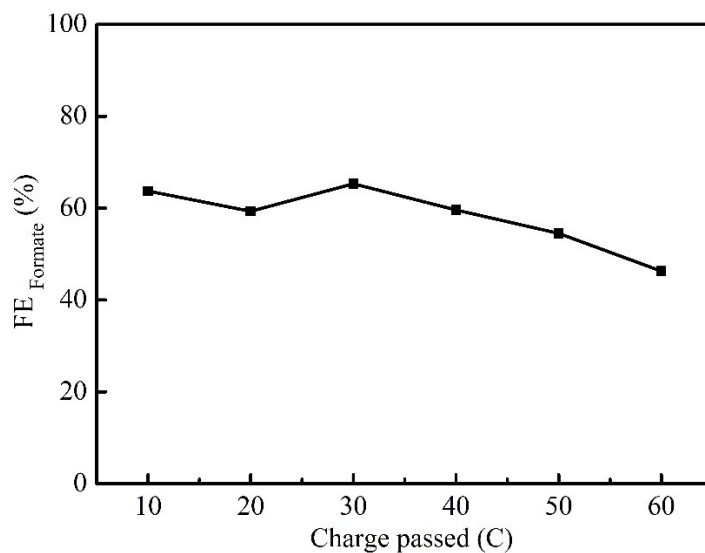


Figure S16. FEs of glucose oxidation to formate on Sn electrode with different charges passed.

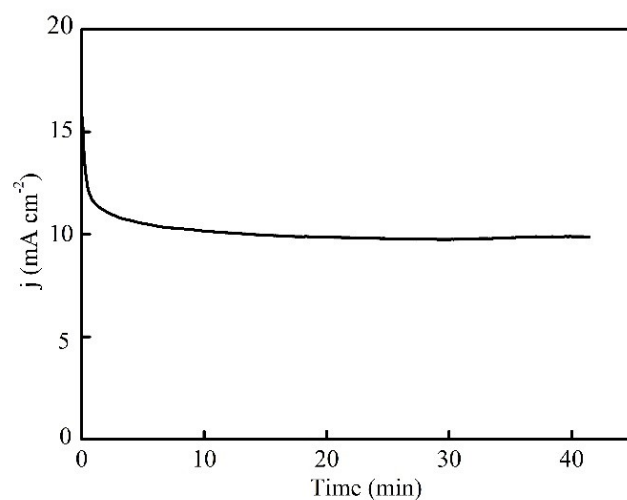


Figure S17. Stability of Sn electrode for oxidation of glucose to formate at 1.17 V vs. RHE.

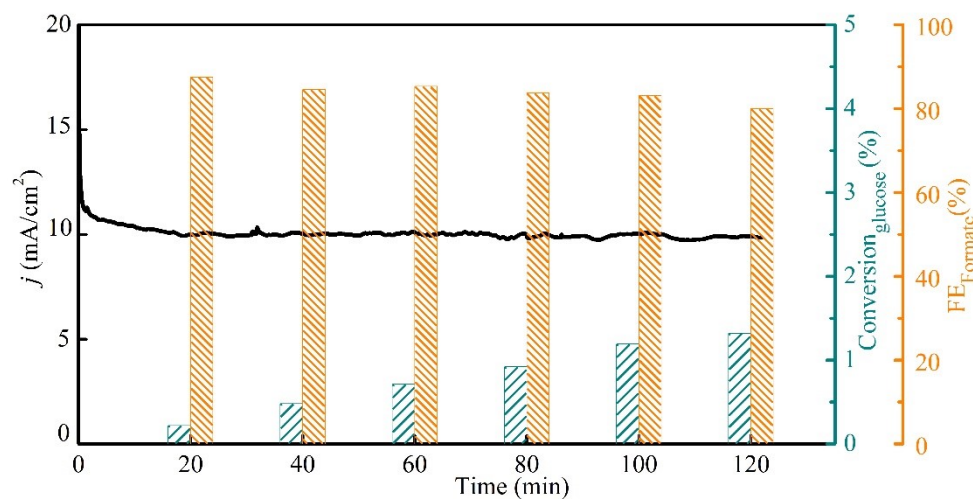


Figure S18. Stability of Sn-SnS_x electrode for oxidation of glucose to formate at 1.1 V vs. RHE.

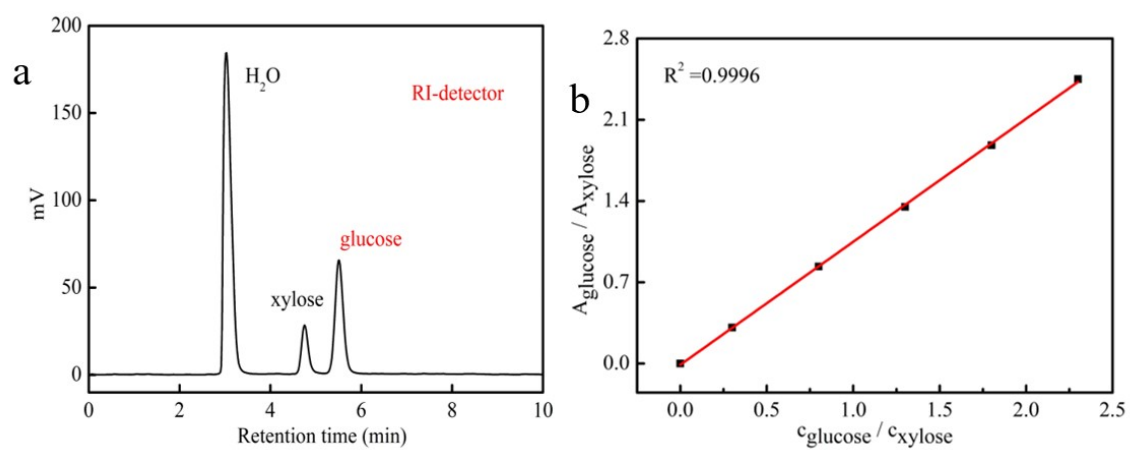


Figure S19. The spectra of glucose detected by HPLC (a), Calibration curve for glucose (b).

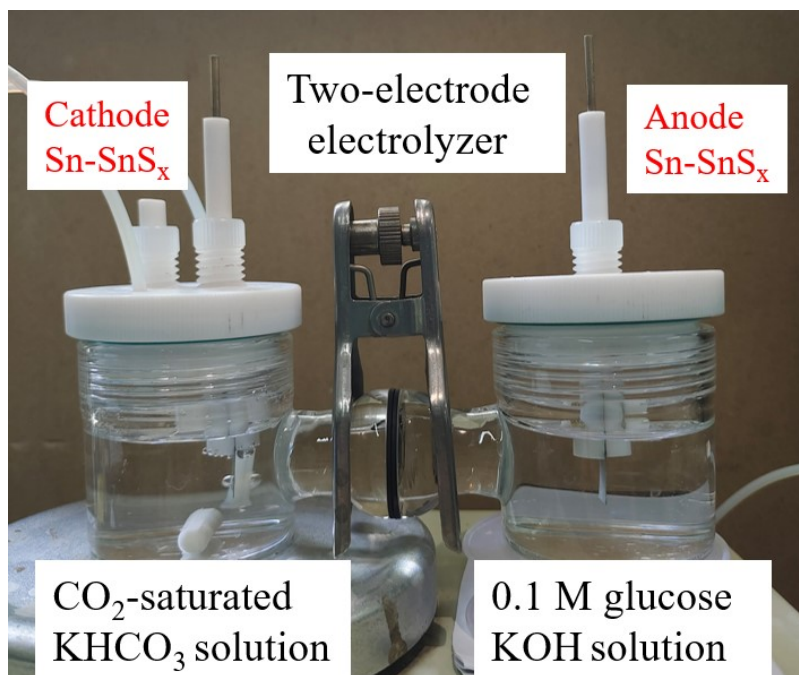


Figure S20. Photograph of the two-electrode cell used for investigating the coupled cathodic CO₂ reduction reaction and anodic glucose oxidation reaction, utilizing the Sn-SnS_x electrode in both cells. The two-electrode electrolyzer consisted of 0.1 M KHCO₃ in the cathode cell and a solution of 0.1 M KOH mixed with 0.1 M glucose in the anode cell, which was separated by a Nafion 117 membrane.

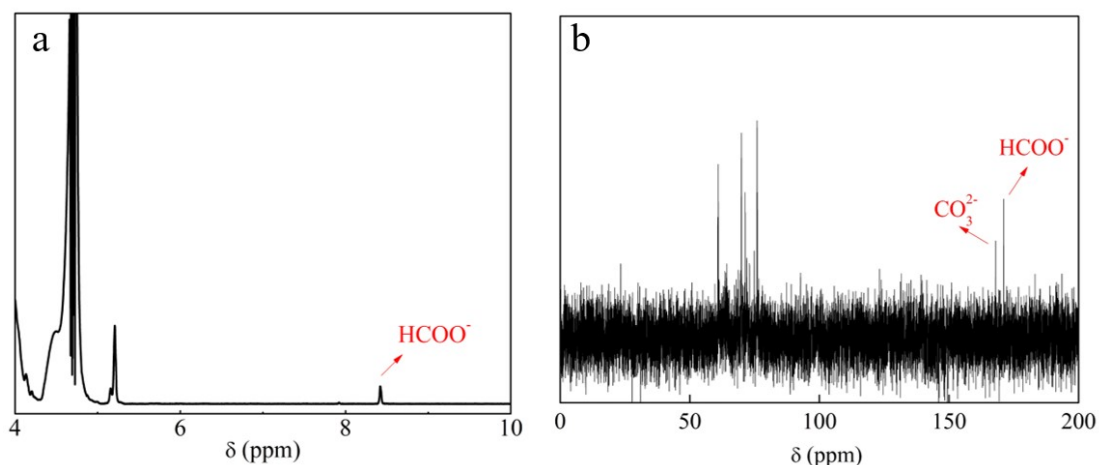


Figure S21. ¹H NMR spectrum (a) and ¹³C NMR spectrum of the anode electrolyte of the CO₂RR//GOR system after half an hour of reaction at 2.2V voltage.

Table S1. The elemental contents of Sn, S calculated from the XPS and TEM-EDX

	Sn (At. %)	S (At. %)
XPS	65.3	34.7
TEM-EDX	75.6	24.4

Table S2. Content of elements in Sn-SnS_x catalyst determined by inductively coupled plasma optical emission spectrometer (ICP-OES).

Catalyst	Sn (wt %)	S (wt %)
Sn-SnS _x	96.9	3.1

Table S3. Performance comparison of CO₂ reduction to formate with tin-based catalysts

Electrocatalyst	Stability (h)	FE _{Formate} (%)	j_{Formate} (mA cm ⁻²)	Reference
Sn quantum sheet	50	60	7.2	2
Sn-pNWs	15	86.2	6.2	3
Cu _{6,26} Sn ₅	10	92.5	8.5	4
Sn ₉₅ -Co ₅ /Cu-f	12	72.2	22.12	5
Nano-SnO ₂ graphene	18	93	8.9	6
SnO ₂ -CNT	10	76.3	8	7
SnO ₂ /CA-80	12	76	16	8
Sn/SnO _x	12	89.6	11.2	9
SnO _x /AgSn	25	80	12.8	10
Bi ₃ S-SnO ₂	1.5	55.6	9.33	11
1%Sb-SnS ₂ nanosheet	8	90.9	5.5	12
SnS ₂ /Sn/rGO	14	84.5	13.9	13
SnS/Sn-NSC NHs	9	91	5	14
Sn-SnS _x	36	93.3	18.6	this work

Table S4. Performance comparison of biomass oxidation to formate

Reactant	Electrocatalyst	ΔE (mV)	FE _{Formate} (%)	Reference
----------	-----------------	-----------------	---------------------------	-----------

raw sugarcane juice	CoNi LDH	229	79.4	15
glucose	Cr-NiFe/NF	34	79.1	16
glucose	NiFe/NF	24	69.1	16
methanol	Co ₃ O _{4-x} /NF-P	200	90	17
xylose	NiCoP	280	68.6	18
glucose	Sn-SnS _x	400	88.5	this work

Table S5: Reduction potential calculations under operating conditions of the two-electrode configuration.

Reaction potential, E (Vvs.NHE)	Calculation	Reference values ^a
$E_{\text{CO}_2/\text{formate}}$	$E = -0.25 - 0.059 \times 6.7 = -0.65$	$E_{\text{CO}_2/\text{formate}}^0 = -0.25\text{V vs. RHE}$ ^{19, 20}
$E_{\text{glucose}/\text{formate}}$	$\Delta G_{\text{rxn}}^0 = \Delta G_f^0(\text{glucose}) - \Delta G_f^0(\text{formate})$ $= -557.6 \text{ kJ/mol}$ $E = 0.48 - 0.059 \times 12.3 = -0.24$	$\Delta G_f^0(\text{glucose}) = -919 \text{ kJ/mol}$ ²¹ $\Delta G_f^0(\text{formate}) = -361.4 \text{ kJ/mol}$ ²¹

^a Values for glucose and formate reported under standard conditions of 1 bar and 298 K.

Table S6. Performance comparison of coupling of anode and cathode to produce formate

Reactant	Anode		Cathode		Cell voltage (V)	Anode FE _{Formate} (%)	Cathode FE _{Formate} (%)	Reference
	Electrode	Reactant	Electrode	Reactant				
ethylene glycol	NiCo ₂ O ₄ /CFP	CO ₂	Sn&SnO ₂ /CC		1.90	85	70	22
methanol	CuONS/CF	CO ₂	mSnO ₂ /CC		1.22	91.3	80.5	23
glycerol	CoP/NF	CO ₂	Ag/BOC		2.2	82.4	47.6	24
glycerol	Ni _x B/NF	CO ₂	BiOBr/NF		/	45	96	25
glucose	Sn-SnS _x	CO ₂	Sn-SnS _x		1.80	87.4	93.9	this work

References

- 1 M. A. Bajada, S. Roy, J. Warnan, K. Abdiaziz, A. Wagner, M. M. Roessler and E. Reisner, *Angew. Chem. Int. Ed.*, 2020, **59**, 15633-15641.
- 2 F. Lei, W. Liu, Y. Sun, J. Xu, K. Liu, L. Liang, T. Yao, B. Pan, S. Wei and Y. Xie, *Nat. Commun.*, 2016, **7**, 12697.
- 3 B. Kumar, V. Atla, J. P. Brian, S. Kumari, T. Q. Nguyen, M. Sunkara and J. M. Spurgeon, *Angew. Chem. Int. Ed.*, 2017, **56**, 3645-3649.
- 4 D. Li, L. Huang, Y. Tian, T. Liu, L. Zhen and Y. Feng, *Appl. Catal. B Environ. Energy*, 2021, **292**, 120119.
- 5 Q. Hu, M. Xu, S. Hu, P.-L. Tremblay and T. Zhang, *J. Electroanal. Chem.*, 2020, **877**, 114623.
- 6 S. Zhang, P. Kang and T. J. Meyer, *J. Am. Chem. Soc.*, 2014, **136**, 1734-1737.
- 7 K. Pavithra and S. M. S. Kumar, *Catal. Sci. Technol.*, 2020, **10**, 1311-1322.
- 8 J. Yu, H. Liu, S. Song, Y. Wang and P. Tsiakaras, *Appl. Catal. A: Gen.*, 2017, **545**, 159-166.
- 9 Q. Lai, W. Yuan, W. Huang and G. Yuan, *Appl. Surf. Sci.*, 2020, **508**, 145221.
- 10 W. Luc, C. Collins, S. Wang, H. Xin, K. He, Y. Kang and F. Jiao, *J. Am. Chem. Soc.*, 2017, **139**, 1885-1893.
- 11 Y. Li, H. Yang, X. Hu, H. Tian, M. Gao, D. Zhang, Z. Li and D. Yang, *ChemElectroChem*, 2019, **6**, 3782-3790.
- 12 L. Yan, Z. Wu, C. Li and J. Wang, *J. Ind. Eng. Chem.*, 2023, **123**, 33-40.
- 13 F. Li, L. Chen, M. Xue, T. Williams, Y. Zhang, D. R. MacFarlane and J. Zhang, *Nano Energy*, 2017, **31**, 270-277.
- 14 S. Zhao, Y. Qin, T. Guo, S. Li, X. Liu, M. Ou, Y. Wu and Y. Chen, *ACS Appl. Nano Mater.*, 2021, **4**, 2257-2264.
- 15 Y. Liu, Z. Chen, Y. Yang, R. Zou, B. Deng, L. Zhong, K. P. Loh and X. Peng, *Appl. Catal. B Environ. Energy*, 2023, **331**, 122559.
- 16 N. Wei, S. Zhang, X. Yao, J. Yang, V. Nica and Q. Zhou, *Sci. China Mater.*, 2023, **66**, 4650-4662.
- 17 J. Zhang, Y. Hua, H. Li, X. Zhang, C. Shi, Y. Li, L. Di and Z. Wang, *Chem. Eng. J.*, 2023, **478**, 147288.
- 18 Y. Yang, R. Zou, J. Gan, Y. Wei, Z. Chen, X. Li, S. Admassie, Y. Liu and X. Peng, *Green Chem.*, 2023, **25**, 4104-4112.
- 19 J. E. Pander, J. W. J. Lum and B. S. Yeo, *J. Mater. Chem. A*, 2019, **7**, 4093-4101.
- 20 J. L. White, M. F. Baruch, J. E. Pander, Y. Hu, I. C. Fortmeyer, J. E. Park, T. Zhang, K. Liao, J. Gu, Y. Yan, T. W. Shaw, E. Abelev and A. B. Bocarsly, *Chem. Rev.*, 2015, **115**, 12888-12935.
- 21 S. Verma, S. Lu and P. J. A. Kenis, *Nat. Energy*, 2019, **4**, 466-474.
- 22 J. Wang, X. Li, M. Wang, T. Zhang, X. Chai, J. Lu, T. Wang, Y. Zhao and D. Ma, *ACS Catal.*, 2022, **12**, 6722-6728.
- 23 X. Wei, Y. Li, L. Chen and J. Shi, *Angewandte Chemie International Edition*, 2020, **60**, 3148-3155.
- 24 X. Guo, S.-M. Xu, H. Zhou, Y. Ren, R. Ge, M. Xu, L. Zheng, X. Kong, M. Shao, Z. Li and H. Duan, *ACS Catal.*, 2022, **12**, 10551-10559.
- 25 J. R. C. Junqueira, D. Das, A. Cathrin Brix, S. Dieckhöfer, J. Weidner, X. Wang, J. Shi and W. Schuhmann, *ChemSusChem*, 2023, **16**, 12697.